

# Simulations of three-dimensional viscoelastic flows past a circular cylinder at moderate Reynolds numbers

DAVID RICHTER, GIANLUCA IACCARINO  
AND ERIC S. G. SHAQFEH†

Department of Mechanical Engineering, Stanford University, Stanford, CA 94305, USA

(Received 8 May 2009; revised 7 December 2009; accepted 16 December 2009;  
first published online 29 March 2010)

The results from a numerical investigation of inertial viscoelastic flow past a circular cylinder are presented which illustrate the significant effect that dilute concentrations of polymer additives have on complex flows. In particular, effects of polymer extensibility are studied as well as the role of viscoelasticity during three-dimensional cylinder wake transition. Simulations at two distinct Reynolds numbers ( $Re = 100$  and  $Re = 300$ ) revealed dramatic differences based on the choice of the polymer extensibility ( $L^2$  in the FENE-P model), as well as a stabilizing tendency of viscoelasticity. For the  $Re = 100$  case, attention was focused on the effects of increasing polymer extensibility, which included a lengthening of the recirculation region immediately behind the cylinder and a sharp increase in average drag when compared to both the low extensibility and Newtonian cases. For  $Re = 300$ , a suppression of the three-dimensional Newtonian mode B instability was observed. This effect is more pronounced for higher polymer extensibilities where all three-dimensional structure is eliminated, and mechanisms for this stabilization are described in the context of roll-up instability inhibition in a viscoelastic shear layer.

---

## 1. Introduction

The numerical study of viscoelastic flows has become a very important source of insight into the physical processes that govern the interaction between polymer additives and the structure of complex fluid motion. Adding dilute concentrations of polymer can drastically alter the characteristics of the fluid flow, therefore many different applications have sought to exploit this phenomenon by better understanding the dynamics of polymer solutions within different flow regimes. A recent, well-known example is turbulent skin friction drag reduction, an effect that has been experimentally observed for over 50 years, but only over the past decade has a large body of numerical simulations truly answered the underlying questions of how turbulent flow is altered by the presence of polymers (Sureshkumar, Beris & Handler 1997; Sibilla & Baron 2002; Dubief *et al.* 2004, 2005; Dimitropoulos *et al.* 2005, 2006; Gupta, Sureshkumar & Khomami 2005; Li, Sureshkumar & Khomami 2006). For instance, Dubief *et al.* (2005) revealed reductions in wall-normal fluctuations in areas correlated with high polymer stretch, suggesting energy extraction by the polymer

† Email address for correspondence: esgs@stanford.edu

from the near-wall vortical structures. This removal of turbulent energy from the flow field and the following deposition of that energy into near-wall high-speed streaks also uncovered a self-regeneration cycle that sustains the turbulence but at the same time reduces the skin friction. Knowledge gained from these types of studies can aid in the better design of solution injectors and experimental set-ups, and eventually allow for the feasibility of new applications to be evaluated.

The existing turbulent drag reduction studies, however, are limited in their scope. These studies, which make up a significant fraction of all high-Reynolds-number viscoelastic flow simulations to date, have been confined to Cartesian grids, focusing primarily on flow through plane channels or over flat plates (Sureshkumar & Beris 1995; Sureshkumar *et al.* 1997; Dimitropoulos, Sureshkumar & Beris 1998; Dubief *et al.* 2004). Furthermore, studies which do simulate three-dimensional viscoelastic flows at high Reynolds numbers, such as that done by Ma, Symeonidis & Karniadakis (2003), are very few in number. Therefore, many of the same underlying questions surrounding polymer interaction with flow features still remain unanswered for more complex types of flow. For this reason, the current investigation will focus on simulating a canonical bluff-body flow: viscoelastic flow around a circular cylinder at moderate Reynolds numbers.

Many studies spanning a wide parameter space have been devoted to studying viscoelastic flow over a cylinder. For the creeping flow (zero-Reynolds-number) limit, a large body of literature exists for theoretical (Ultman & Denn 1971; Mena & Caswell 1974), experimental (Broadbent & Mena 1974; Manero & Mena 1981; McKinley, Armstrong & Brown 1993) and numerical (Townsend 1980; Chilcott & Rallison 1998; Liu *et al.* 1998; Phan-Thien & Dou 1999) investigations. Much of the focus of these and similar studies are the purely elastic instabilities which occur at moderate-to-high Weissenberg numbers of inertialess viscoelastic flows past cylinders, arrays of cylinders and spheres. Because of the form of the governing equations in the zero-Reynolds-number limit (nonlinear convection neglected), the numerical simulation of these types of flows usually involves finite element techniques, finite volume techniques, or some hybrid of the two, and has been performed so many times for such a wide variety of non-Newtonian constitutive models that creeping flow past a cylinder is commonly used as a validation test case (Oliveira, Pinho & Pinto 1998; Fan, Tanner & Phan-Thien 1999; Wapperom & Webster 1999; Ma *et al.* 2003). However, since the low-Reynolds-number regime is not the primary focus of the present discussion, the details of these studies will not be given here.

For the case of finite-Reynolds-number viscoelastic flow over a cylinder, the majority of the literature consists of experimental investigations and only recently have numerical simulations been performed. Early experiments done by Gadd (1966) showed a significant decrease in the vortex shedding frequency due to viscoelasticity at a Reynolds number of roughly 240. Gadd (1966) further demonstrated that the fluid elasticity is responsible for this reduction, since solutions of inelastic guar gum exhibited no frequency change. These findings were supported by the experiments performed by Kalashnikov & Kudin (1970), who observed shedding frequency reduction for viscoelastic polyethylene oxide (PEO) solutions at slightly lower Reynolds numbers. However, for degraded (inelastic) solutions of PEO and inelastic guar gum solutions, either no change or only slight increases in the Strouhal number were seen. Usui, Shibata & Sano (1980) later experimentally showed the same decrease in Strouhal number for  $100 < Re < 300$ , empirically determining that the difference  $St_{Newtonian} - St_{viscoelastic} \sim Wi^{0.32}$ . Moreover, these researchers also showed

that for dilute PEO solutions the magnitude of the reduction in  $St$  increased with polymer concentration.

One of the first experimental studies to comment on the drag behaviour of inertial viscoelastic flows over cylinder was that of James & Gupta (1971). In their experiments, they showed that for several different blends of Polyox WSR brand PEO at Reynolds numbers below 200, the drag was actually higher (the magnitude of the increase depending on the polymer used) than the corresponding value for Newtonian flow. They then showed that for a single blend, solutions with different concentrations all collapsed to one drag curve when plotted against  $D^2/\lambda v = Re/Wi = 1/E$  (where  $E$  is the elasticity parameter  $E \equiv Wi/Re$ ). Somewhat contrary to this work, however, were the results from Kato & Mizuno (1983) a decade later, showing that the form drag for low Reynolds number stayed roughly equal to the Newtonian case for various concentrations and that at high Reynolds number ( $2000 < Re < 10\,000$ ), form drag reductions of up to 33% can be seen for certain types and concentrations of PEO solutions. Furthermore, by measuring angular pressure distributions along the cylinder surface, the cause of the drag reduction and the reduction in shedding frequency are argued to be due to a rise in back pressure and a delay in separation, respectively. For polymer solutions with slightly different shear thinning characteristics, the same rise in back pressure and resulting reduction in form drag was seen by Coelho & Pinho (2004) for carboxymethyl cellulose (CMC) and methyl hydroxyethyl cellulose (brand name tylose) solutions; however, this was accompanied by an increase in vortex shedding frequency, contrary to previous experiments. This difference was explained by their own previous experiments (Coelho & Pinho 2003*a,b*) as resulting from the opposite response of the flow to fluid elasticity and shear thinning (elasticity tending to decrease the vortex shedding frequency while shear thinning tending to increase it). The fluids used in all of their experiments exhibited a stronger effect due to shear thinning.

Another striking feature of viscoelastic cylinder flow at finite Reynolds numbers is the ability of polymer solutions to suppress instabilities in the wake. This effect presents itself in many different forms, one of which is illustrated by a lengthening of the recirculation bubble behind the cylinder. Previous studies on the stability of viscoelastic free shear layers have demonstrated the suppression of Kelvin–Helmholtz type instabilities. Viscoelasticity shifts the Kelvin–Helmholtz instabilities to larger wavenumbers and reduces the growth rate (see Azaiez & Homsy 1994*a,b*; Kumar & Homsy 1999). In the context of flow over a cylinder, the shear layers that surround the recirculation zone behind the cylinder are consequently lengthened due to the slower growth of the instability leading to vortex formation. This qualitative effect has been seen numerous times both in experiments and in numerical simulations (Cadot & Lebey 1998; Cadot & Kumar 2000; Oliveira 2001; Coelho & Pinho 2003*b*; Sahin & Owens 2004). Further demonstrating the stabilizing effect of viscoelasticity in the wake are the experiments of Cressman, Bailey & Goldberg (2001), who concluded that the fluid extensional viscosity is responsible for the suppression of transverse velocity fluctuations in the cylinder wake. Since these velocity fluctuations presumably excite the instability modes in the shear layer, their suppression is consistent with the notion that vortex formation should be delayed.

Another indication of stabilization due to viscoelasticity is its effect on the various critical Reynolds numbers which delineate the different cylinder flow regimes. In their detailed study on viscoelastic cylinder flow stability, Pipe & Monkewitz (2006) found that as either the elasticity number  $E = Wi/Re$  or the polymer concentration increases, the critical Reynolds number for the onset of vortex formation increases

nearly linearly. They too measure a reduction in transverse velocity fluctuations at high concentrations, suggesting again that a dilute concentration of polymers can delay the growth of instabilities. Similar results are obtained by Sahin & Owens (2004), who performed a linear stability analysis as well as numerical simulations to quantitatively show an increase in the critical Reynolds number marking the onset of vortex shedding. At higher Reynolds numbers, transitions beyond the onset of vortex shedding that occur have been extensively characterized for Newtonian flow (see Williamson 1996*b* for a summary), and these are also affected by the presence of viscoelasticity. Cadot & Kumar (2000) focused on the interaction of polymer additives with three-dimensional instabilities and revealed a near complete suppression of the spanwise mode A instabilities that characterize the first modes of three-dimensional cylinder flow transition (Williamson 1996*a*). A few years later, for shear thinning (less elastic) fluids, Coelho & Pinho (2003*a,b*) actually observed a reduction in the critical Reynolds numbers characterizing the end of the transition regime and the beginning of the shear layer transition.

As mentioned previously, the large majority of viscoelastic cylinder flow studies at finite Reynolds number have involved experimental techniques, while numerical investigations are few in number. The most recent of these are that of Oliveira (2001) and Sahin & Owens (2004), who both utilize the modified FENE-CR rheological model to compute viscoelastic flow over a cylinder at finite Reynolds numbers. In both studies, reductions in Strouhal number, decreases in drag and lengthening of the recirculation region are all observed and are consistent with most previous experiments, and insight is gained into how polymeric additives can influence the flow features. After confirming results with these existing studies, it is the objective of this investigation to build upon the knowledge gained from these works and to discuss interesting new phenomena which occur for the FENE-P constitutive model at larger Reynolds numbers and higher polymer extensibilities.

## 2. Problem formulation

### 2.1. Governing equations

For an incompressible fluid in the presence of polymer additives, the dimensionless governing equations are obtained by enforcing conservation of mass and momentum on a differential fluid element:

$$\frac{\partial u_j}{\partial x_j} = 0, \quad (2.1)$$

$$\frac{\partial u_i}{\partial t} + u_j \frac{\partial u_i}{\partial x_j} = -\frac{\partial p}{\partial x_i} + \frac{\beta}{Re} \frac{\partial^2 u_i}{\partial x_j \partial x_j} + \frac{1-\beta}{Re} \frac{1}{Wi} \frac{\partial \tau_{ij}^p}{\partial x_j}. \quad (2.2)$$

These expressions closely resemble the dimensionless Navier–Stokes equations for incompressible Newtonian flow with the exception of the polymer stress  $\tau_{ij}^p$ , a term which represents the additional body stresses due to the elasticity of the polymers in the flow. To describe the degree of viscoelasticity, the Weissenberg number,  $Wi = \lambda U_\infty / D$ , is defined as the ratio of a characteristic polymer relaxation time scale  $\lambda$  and a characteristic flow time scale  $U_\infty / D$ , where for this case  $D$  is the cylinder diameter. The Reynolds number,  $Re = \rho D U_\infty / (\mu_s + \mu_p)$ , is a ratio of inertial forces to viscous forces, and  $\beta$ ,  $\beta = \mu_s / (\mu_s + \mu_p)$ , refers to the ratio of the zero-shear-rate viscosity of the solvent to the zero-shear-rate viscosity of the total solution ( $\mu_s$  is the viscosity contribution from the solvent,  $\mu_p$  is the viscosity contribution from the polymer).

In order to close this system of equations, a model for the polymer stress must be introduced, and for this work the molecular-based FENE-P model is employed. This model approximates an individual member of a dilute concentration of polymers as a single dumbbell connected with a finitely extensible nonlinear elastic spring, and through a balance of forces acting on the beads, an expression for the polymeric stress  $\tau_{ij}^p$  can be determined using kinetic theory (see Bird, Armstrong & Hassager 1987):

$$\tau_{ij}^p = \frac{c_{ij}}{1 - \frac{c_{kk}}{L^2}} - \delta_{ij}. \quad (2.3)$$

In this equation,  $L$  refers to the maximum polymer extensibility, which is non-dimensionalized by the equilibrium length of a linear spring  $((kT/H)^{1/2})$  where  $T$  is the absolute temperature,  $k$  is Boltzmann's constant and  $H$  is the Hookean spring constant for an entropic spring. Also,  $c_{ij}$  represents the averaged polymer conformation tensor (also scaled by the equilibrium Hookean spring length), which is defined as the preaveraged diadic product of the polymer end-to-end vector and is governed by the hyperbolic transport equation shown below (for discussion of the mathematical character of the FENE-P fluid equation, see Purnode & Legat 1996).

$$\frac{\partial c_{ij}}{\partial t} + u_k \frac{\partial c_{ij}}{\partial x_k} - c_{ik} \frac{\partial u_j}{\partial x_k} - c_{kj} \frac{\partial u_i}{\partial x_k} = -\frac{1}{Wi} \tau_{ij}^p. \quad (2.4)$$

The FENE-P model is chosen for this work based on its ability to properly represent the finite extensibility, and thus the bounded stress, of the polymers. For problems with large  $Wi$  and large strain rates, this feature is required in order to obtain bound solutions, and linear springs such as the Oldroyd-B constitutive model cannot be faithfully used. Moreover, the FENE-P model has been used in many previous studies involving high-Reynolds-number viscoelastic flows, and its ability to provide accurate physical insight into these types of problems has been demonstrated (see Azaiez & Homsy 1994b; Sureshkumar *et al.* 1997; Kumar & Homsy 1999; Dubief *et al.* 2004, 2005; Dimitropoulos *et al.* 2005, 2006).

Because the polymer conformation tensor  $c_{ij}$  is symmetric, these make up a set of 10 coupled partial differential equations that, when solved properly, provide the instantaneous velocity, pressure, polymer conformation and non-Newtonian stress fields of a fluid with a dilute concentration of polymer additives. One point to note is that one of the underlying suppositions is the 'ocean of polymer' approximation, which assumes a uniform polymer concentration throughout the flow domain. In certain cases this can be inappropriate, and using a method previously formulated, an additional scalar transport equation for the polymer concentration can be coupled into the above equations if desired (Dimitropoulos *et al.* 2006).

## 2.2. Numerical method

To solve these equations numerically, the viscoelastic code was built upon an existing incompressible Newtonian flow solver developed at Stanford's Centre for Turbulence Research. This solver, named CDP (after the late Charles David Pierce), is based on an unstructured finite volume formulation and is capable of computing over many processors in parallel. To account for the presence of viscoelasticity, the polymer stress term has been added to the momentum equation solver as a volumetric source term, while the conformation tensor evolution equation is solved as six coupled scalar transport equations.

First, a brief description of the underlying flow solver will be given, followed by the details of the viscoelastic portion. As previously mentioned, the code is based

on an unstructured formulation, thus the finite volume method is used to compute collocated, node-based solutions to the governing mass and momentum equations. All linear terms in the governing momentum equations are advanced simultaneously in time using the semi-implicit Crank–Nicholson method, while the nonlinear convection term is linearized and solved with a combination of Crank–Nicholson and Adams–Bashforth discretizations. Spatial derivatives for the fluid velocity  $u_i$  are approximated using central differencing. To enforce mass conservation, a corrector step is performed after solving the momentum equations which uses an advanced multi-grid technique to solve the pressure Poisson equation, thus providing a solenoidal velocity field which also satisfies the momentum equations. Further details can be found in previous publications (see Ham & Iaccarino 2004; Mahesh, Constantinescu & Moin 2004; Ham, Mattsson & Iaccarino 2006).

The divergence of the additional viscoelastic source term of the momentum equations is computed using the most updated values of the conformation tensor  $c_{ij}$ . One special note on handling this term is that for consistency, the divergence operator is computed by using the chain rule on the right-hand side of (2.3) such that the extra stress is written entirely in terms of the conformation tensor  $c_{ij}$  and its derivatives:

$$\begin{aligned} \frac{\partial \tau_{ij}^p}{\partial x_j} &= \frac{\partial}{\partial x_j} \left[ \frac{c_{ij}}{1 - \frac{c_{kk}}{L^2}} - \delta_{ij} \right], \\ &= \frac{\left(1 - \frac{c_{kk}}{L^2}\right) \frac{\partial c_{ij}}{\partial x_j} - c_{ij} \frac{\partial}{\partial x_j} \left(1 - \frac{c_{kk}}{L^2}\right)}{\left(1 - \frac{c_{kk}}{L^2}\right)^2}. \end{aligned} \quad (2.5)$$

This is done since  $c_{ij}$  is the transported variable, and because the condition of  $\tau_{ij}^p$  at the domain boundaries (particularly at the walls) is never specified, its derivative cannot be calculated near the edges of the domain without additional information about the polymer stress at the boundary.

For the conformation tensor evolution equation, the components  $c_{ij}$  are advanced in time prior to solving the momentum equations. Since the polymer stress of the FENE-P model becomes singular as the trace of the conformation tensor  $c_{kk}$  approaches the square of polymer maximum extensibility  $L^2$ , careful attention must be paid to the time advancing technique so as not to overstretch a polymer beyond its maximum extension. As a result, a modified version of the novel method proposed by Dubief *et al.* (2005) is used to advance the trace of the conformation tensor independently of the individual components in a way that assures boundedness of the polymer stretch  $c_{kk}$ . A brief description of this method will be given here.

First, contracting (2.4) provides an evolution equation for the conformation tensor trace  $c_{kk}$ :

$$\frac{\partial c_{kk}}{\partial t} = R_{kk} - \frac{1}{Wi} \left( \frac{c_{kk}}{\psi} - 3 \right). \quad (2.6)$$

In this equation,  $\psi$  is defined as the term which appears in the denominator of the polymer stress:

$$\psi = 1 - \frac{c_{kk}}{L^2}, \quad (2.7)$$

and  $R_{kk}$  represents the contributions from both the advection term as well as the upper convected derivative terms:

$$R_{kk} = -u_j \frac{\partial c_{kk}}{\partial x_j} + c_{kj} \frac{\partial u_k}{\partial x_j} + c_{jk} \frac{\partial u_k}{\partial x_j}. \quad (2.8)$$

Discretizing (2.6) in time using Crank–Nicholson for the singular term ( $c_{kk}/\psi$ ) and treating all components of  $R_{kk}$  explicitly, a quadratic equation for  $\psi$  that only depends on known values is obtained:

$$(\psi^n)^2 - \psi^n \left( \psi^{n-1} - \frac{\Delta t}{L^2} R_{kk}^{n-1} - \frac{\Delta t}{2Wi} + \frac{\Delta t}{2Wi} \frac{(1 - \psi^{n-1})}{\psi^{n-1}} - \frac{3\Delta t}{L^2 Wi} \right) - \frac{\Delta t}{2Wi} = 0. \quad (2.9)$$

In this equation, superscript  $n$  refers to the current time level and  $n - 1$  refers to the previous time level where all quantities, notably  $R_{kk}$ , are considered known. As pointed out in Dubief *et al.* (2005), it is trivial to show that the roots of (2.9) are always non-zero, real and opposite in sign. Therefore, by choosing the positive root for  $\psi$ , it is guaranteed that  $c_{kk}/L^2 < 1$  and thus that the conformation tensor trace and the polymer stress will always remain upper bounded.

By solving this equation for the new value of  $\psi$  at the beginning of a time step, before solving either the individual conformation tensor component equations or the momentum equations, the denominator of the polymer stress  $\tau_{ij}^p$  is considered known throughout a given time step. To solve the evolution equations for the conformation tensor components, all terms are again advanced in time with the Crank–Nicholson method and scalar derivatives are now approximated using a quadratic upwind interpolation for convective kinematics (QUICK) discretization.

Since the six conformation tensor component equations are coupled not only to each other, but also to the momentum equations, inner iterations can be performed within a time step to achieve consistent values of both velocity and polymer conformation. For  $k$  inner iterations, the scalar transport equations, the momentum equations and the pressure equation are all solved  $k$  times, using averaged values (between a given time step's original and most recently calculated values) for coupled terms appearing in the equations. The extra bounding step of advancing  $c_{kk}$  is not included within an inner iteration, therefore the value calculated at the beginning of the time step is used throughout.

One more point to note is that due to the hyperbolic nature of the conformation tensor evolution equation, sharp gradients of polymer stress can theoretically form, and like with shocks in compressible fluid flow, these bands can be numerically difficult to resolve. As a result and despite the usage of the QUICK discretization for scalar derivatives, a constant artificial dissipation for the  $c_{ij}$  equations is introduced throughout the entire flow field, implemented by adding an extra diffusion term to the left-hand side of (2.4):

$$\frac{\partial c_{ij}}{\partial t} + u_k \frac{\partial c_{ij}}{\partial x_k} - c_{ik} \frac{\partial u_j}{\partial x_k} - c_{kj} \frac{\partial u_i}{\partial x_k} - \Gamma \frac{\partial^2 c_{ij}}{\partial x_k \partial x_k} = -\frac{1}{Wi} \tau_{ij}^p. \quad (2.10)$$

In (2.10),  $\Gamma$  refers to the constant scalar diffusivity, chosen so that the Schmidt number ( $Sc \equiv \nu/\Gamma$ , the ratio of momentum diffusivity to scalar diffusivity) is about 10 for all cases discussed in this paper. For sake of comparison, previous drag reduction (high  $Re$ ) studies which employ a similar global artificial stress diffusion use Schmidt numbers below a value of 1 (Sureshkumar & Beris 1995; Sureshkumar *et al.* 1997).

The sensitivity of our simulations to this value has been examined and seen to have little effect on the solution when chosen such that  $Sc \geq 10$ .

A quick summary of the numerical procedure through one time step (going from step  $n$  to  $n + 1$ ) is presented below:

(i) Equation for  $c_{kk}$  is advanced in a way that guarantees polymer boundedness and a value for  $\psi^n$  is obtained.

(ii) All six scalar equations for the conformation tensor components are solved sequentially, advanced in time with a Crank–Nicholson scheme and using the value of  $\psi^n$  determined in step (i) in the polymer stress denominator.

(iii) All three momentum equations are solved simultaneously (using the polymer stress divergence calculated with  $c_{ij}$  and its derivatives) and advanced in time with Crank–Nicholson.

(iv) Pressure is determined by solving a Poisson equation and used to correct the velocity field calculated in step (iii).

(v) If inner iterations are present, steps (ii) through step (iv) are repeated.

### 2.3. Problem specification and boundary conditions

The problem definition is that of viscoelastic flow around a circular cylinder at both  $Re = 100$  and  $Re = 300$ . At present, simulations are limited to this moderate-Reynolds-number range due to the large amount of computation time required to probe higher  $Re$ . In general, cylinder flow is rich in physical effects such as shear layers, recirculation regions, boundary layers and vortex dynamics, thus making this problem ideal for studying complex viscoelastic effects. Furthermore, as the Reynolds number is increased, we know that for a Newtonian fluid the flow type changes dramatically, starting from steady laminar flow, changing to unsteady two-dimensional vortex shedding, then going through several stages of three-dimensional transition before finally reaching full turbulence (see Williamson 1996*b*). As a result, these different stages also present opportunities to investigate the effect of viscoelasticity under many different circumstances. Because the Newtonian counterpart has been studied extensively in the past (much of which is reviewed in Williamson 1996*b*), comparisons between Newtonian and non-Newtonian flows can be easily made. For the cases chosen, Newtonian flow at  $Re = 100$  lies within the two-dimensional laminar vortex shedding regime, while the  $Re = 300$  case lies within the initial stages of three-dimensional transition.

For each different case, a slightly different mesh was used to perform the calculations. A schematic of the  $x$ – $y$  plane of the respective domains, denoted by Mesh 1 and Mesh 2, is shown in figure 1. The primary difference between the domains is that for Mesh 2, the downstream exit boundary was extended from  $16.5D$  in Mesh 1 to  $45D$ . Because the fluid motions are purely two-dimensional at a Reynolds number of 100, the spanwise domain length is set at  $1D$  and is discretized using only one cell for all  $Re = 100$  cases. For the larger Reynolds number, however, 64 discretization points were used over a span of  $2\pi D$  in order to accurately capture the three-dimensional behaviour. In both cases, the domain extends radially to  $23D$  upstream of the cylinder. A close up of the spanwise-normal plane of the unstructured mesh surrounding the cylinder is shown in figure 2, and table 1 contains relevant mesh size information.

The boundary conditions applied for all calculations are as follows. It is first useful to note that Mesh 1 contains only two far-field boundaries: a curved inlet to the left of the cylinder and a vertical outlet to the right, while Mesh 2 contains two additional far-field boundaries, referred to in this section as the ‘top’ and ‘bottom’

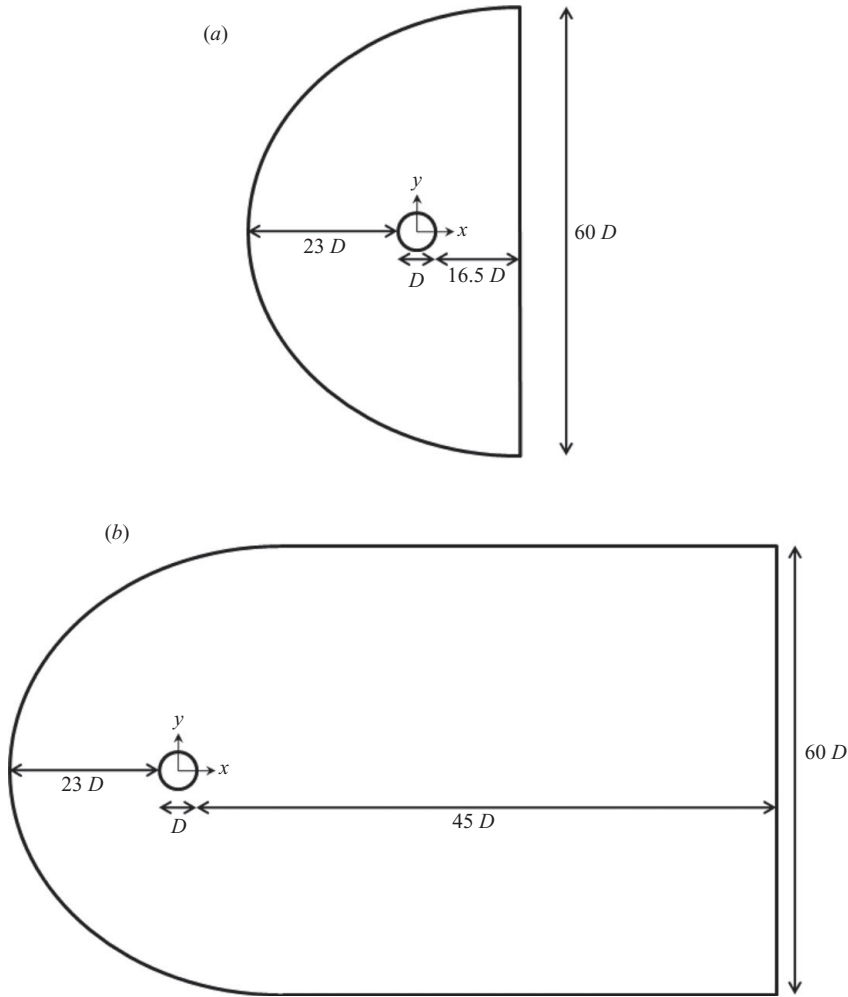


FIGURE 1. Schematic of  $x$ - $y$  domains used for (a) Mesh 1:  $Re = 100$ ,  $L^2 = 100$  cases and (b) Mesh 2:  $Re = 100$ ,  $L^2 = 10\,000$  cases as well as all  $Re = 300$  cases.

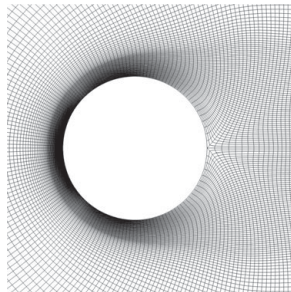


FIGURE 2. Close-up of the  $x$ - $y$  plane of the unstructured mesh used for cylinder calculations.

boundaries. Along the entire inlet, a unit velocity  $U_\infty = [1, 0, 0]$  is assigned, as well as the equilibrium polymer conformation  $c_{ij,\infty} = \delta_{ij}$ . At the domain outlet, a convective outlet condition is applied to both the velocities as well as  $c_{ij}$ . Along the cylinder wall, a no-slip condition is applied for the fluid velocity. In general, the hyperbolic nature

---

Mesh	$N_{nodes}$	$\Delta\theta_{min}$	$\Delta r_{min}$	$\Delta y_{min}$
Mesh 1	96 460	0.02738	0.00149D	0.0172D
Mesh 2	115 580	0.02738	0.00149D	0.0172D

---

TABLE 1. Minimum mesh sizes along cylinder surface ( $\Delta\theta_{min}$  and  $\Delta r_{min}$ ) and along wake centreline ( $\Delta y_{min}$ ).

---

of the  $c_{ij}$  evolution equation would mandate that no condition for  $c_{ij}$  be specified at the wall; however, due to the presence of artificial diffusion, such a condition must be explicitly enforced. Therefore in the present calculations, a no-flux condition is used for  $c_{ij}$  in the normal direction at the cylinder surface ( $\partial c_{ij}/\partial n = 0$ ). For the top and bottom boundaries (in Mesh 2), a zero flux slip condition is used for both velocity and polymer conformation since the boundary is sufficiently far from the cylinder for the flow to be assumed parallel and unaffected by the interior dynamics. Finally, periodic conditions in the spanwise direction are applied for both cases.

### 3. Code verification

#### 3.1. Channel flow comparison

In order to test the validity of the viscoelastic computations, several steps were taken to assess the accuracy of the code. First, a simulation was performed of steady fully developed Poiseuille flow in a two-dimensional channel. For the FENE-P model, an exact solution for the fully coupled viscoelastic problem has been previously derived by Cruz, Pinho & Oliveira (2005), thus providing a direct comparison for the code. For sake of clarity, a description of the derivation is omitted and only the exact dimensionless solution for the present case is provided below.

From the conformation tensor evolution equation (2.4), it is found in Cruz *et al.* (2005) that

$$\tau_{22}^p = \tau_{33}^p = \tau_{13}^p = \tau_{23}^p = 0. \quad (3.1)$$

That is, all components of the polymeric stress  $\tau_{ij}^p$  are zero except for  $\tau_{11}^p$  and  $\tau_{12}^p$  which are given by (3.2) and (3.3).

$$\tau_{12}^{p3} + \frac{L^2}{2} \left( 1 + \frac{3}{L^2} + \frac{(1-\beta)}{\beta} \right) \tau_{12}^p - \frac{L^2}{2} \frac{ReWi}{\beta} \frac{dp}{dx} y = 0, \quad (3.2)$$

$$\tau_{11}^p = 2\tau_{12}^{p2}. \quad (3.3)$$

After solving the cubic equation for  $\tau_{12}^p$  at a given channel height and then using it to obtain  $\tau_{11}^p$ , it immediately follows that the trace of the conformation tensor is given by

$$c_{kk} = \frac{\tau_{11}^p + 3}{1 + \frac{\tau_{11}^p + 3}{L^2}}. \quad (3.4)$$

From the trace  $c_{kk}$ , all individual components of the conformation tensor can then be found:

$$c_{ij} = (\tau_{ij}^p + \delta_{ij}) \left( 1 - \frac{c_{kk}}{L^2} \right). \quad (3.5)$$

Finally, the velocity profile in the channel exhibits a correction from the well-known Newtonian parabolic solution due to the presence of viscoelasticity. By integrating the momentum equation (2.2), the streamwise velocity  $u$  is shown in Cruz *et al.* (2005)

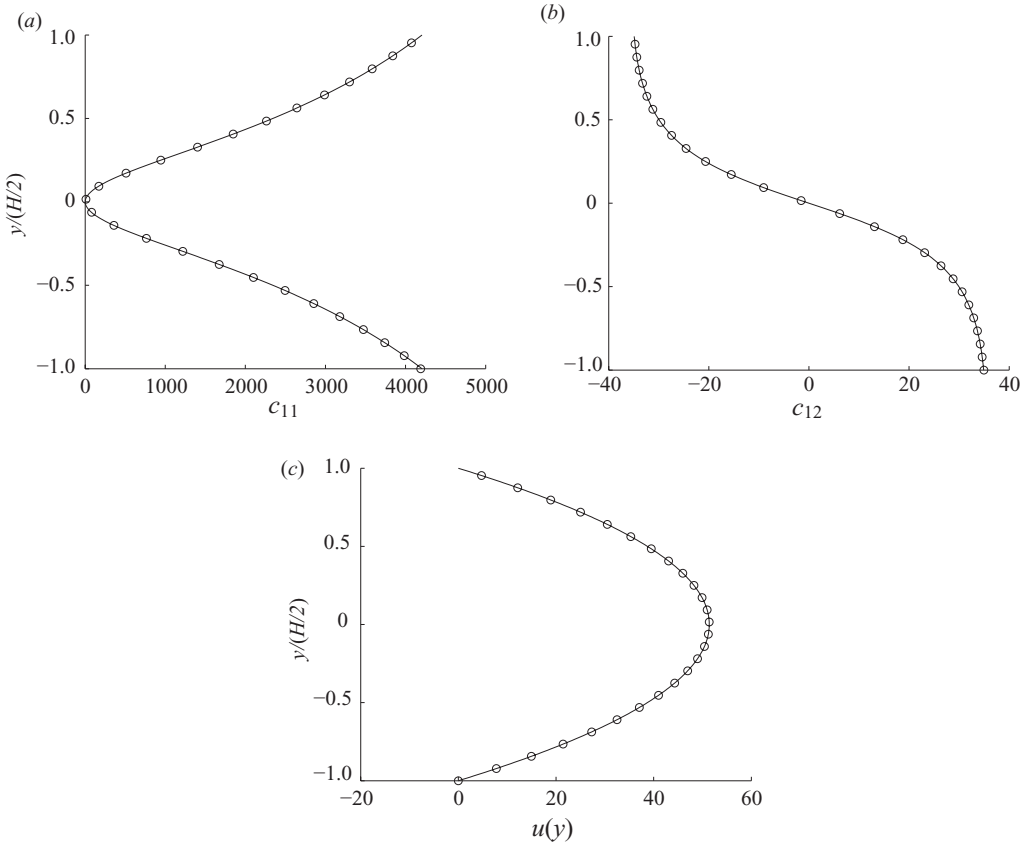


FIGURE 3. Comparisons of analytic (—) and simulated (○) conformation tensor components (a)  $c_{11}$ , (b)  $c_{12}$  and (c) streamwise velocity  $u$  for  $Re = 100$ ,  $Wi = 1.0$ ,  $L^2 = 10\,000$  and  $\beta = 0.9$ .

to vary over the channel height  $y$  as

$$u(y) = \frac{Re}{2\beta} \frac{dp}{dx} (y^2 - 1) \frac{1 - \beta}{\beta Wi} [F^+(H)G^-(H) - F^+(y)G^-(y) + F^-(H)G^+(H) - F^-(y)G^+(y)], \quad (3.6)$$

where, using the same notation in Cruz *et al.* (2005),  $H$  is the channel half-height and

$$F^\pm(X) = \left( CX \pm \sqrt{A^3 + (CX)^2} \right)^{1/3}, \quad (3.7)$$

$$G^\pm(X) = 3CX \pm \sqrt{A^3 + (CX)^2} \quad (3.8)$$

and

$$A = \frac{L^2}{6} \left( 1 + \frac{3(1 - \beta)}{L^2 \beta} \right), \quad (3.9)$$

$$C = \frac{L^2 Re Wi}{4 \beta} \frac{dp}{dx}. \quad (3.10)$$

Simulations were performed for channel flow with  $Re = 100$ ,  $Wi = 1.0$ ,  $L^2 = 10\,000$  and  $\beta = 0.9$ . The comparisons of the conformation tensor component profiles of  $c_{11}$  and  $c_{12}$  as well as the velocity profiles between the numerically calculated values and the analytic solution are shown in figure 3. It is apparent that the solution obtained

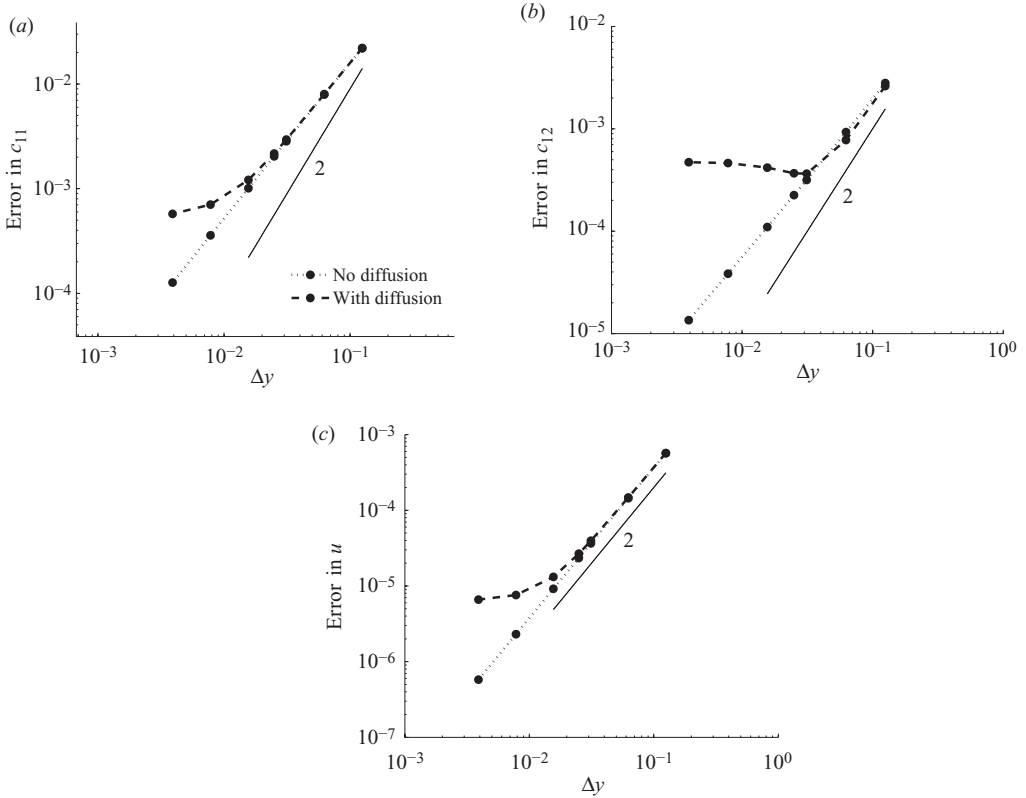


FIGURE 4. Relative error in the  $L_2$  norm of (a)  $c_{11}$ , (b)  $c_{12}$  and (c) streamwise velocity  $u$  for  $Re = 100$ ,  $Wi = 1.0$ ,  $L^2 = 10000$  and  $\beta = 0.9$ .

numerically accurately captures the exact behaviour of the polymer conformation and the solution velocity across the channel height, and furthermore these calculations can be used to compute the order of accuracy of the solver. By successively refining the grid in the channel height direction, error in velocity as well as all components of  $c_{ij}$  was seen to decrease as nearly second order. This is shown in figure 4.

As mentioned previously, global artificial diffusion has been introduced into the conformation tensor evolution equations, and its effect on the convergence rate is also clearly illustrated in figure 4. By comparing the two curves in each plot, it is immediately obvious that at a certain point in the refinement process, error due to artificial diffusion begins to dominate and causes the convergence rate to plateau. Since this occurs with sufficiently small relative error, however, the effect on all subsequent simulations is assumed to be negligible. This assumption was later qualitatively confirmed by observing no visible change in the solution as long as the Schmidt number was maintained at  $O(10)$  or above. Furthermore, based on the findings of Dubief *et al.* (2005), the amount of stress diffusion used presently is not expected to have any deleterious effects on the flow structures or instability mechanisms since its effects on the velocity field are contained to small-scale regions of the velocity spectrum which do not exist for the current Reynolds-number regimes.

One important item to note is that for steady, laminar channel flow, artificial stress diffusivity is actually not required to ensure numerically stable results, therefore making this case a good indicator of the error due to the artificial diffusivity employed in the current simulations. However, for all cylinder flows discussed subsequently (which

have much higher polymer conformation gradients and are all unsteady in time), numerical instabilities do form unless some small amount of diffusion is included.

### 3.2. Cylinder flow comparison

For the case of unsteady cylinder flow, an analytic solution does not exist, even for the Newtonian case. Additionally, because the steady two-dimensional channel flow used above does not exercise all terms of the governing equations, it is not adequate to assume that more complex flow types will be free of other sources of error. Therefore, additional methods of verification were used for the viscoelastic flow over a cylinder, including a quantitative comparison to the simulations of Oliveira (2001) and additional grid convergence studies.

Before discussing the results of this comparison, basic information about the time stepping procedure must be introduced. For all simulations presented in this study, the time step size  $\Delta t$  was chosen based on a CFL (Courant–Friedrichs–Lewy) number of 0.1. Furthermore, for the time-dependent cylinder flows, a stopping condition based on the mean drag was used. When the time-averaged value of the mean did not change appreciably for a desired period of time, the flow was considered statistically steady and data was extracted. Although they are not included here, plotted signals of all relevant quantities were seen to exhibit no visible numerical dissipation in time.

In Oliveira (2001), simulations were performed for a viscoelastic fluid governed by the modified FENE-CR model (or modified Chilcott–Rallison model, FENE-MCR, developed in Coates, Armstrong & Brown 1992) at a Reynolds number of 100 and a Weissenberg number ranging from  $Wi = 0$  (Newtonian) to  $Wi = 80$ .

The FENE-MCR model is derived directly from the FENE-CR model, which itself is derived in an *ad hoc* manner from the FENE-P model (see Bird & Wiest 1995). Whereas the equation governing the conformation tensor for the FENE-P model was shown in (2.4), the FENE-CR evolution equation for  $c_{ij}$  remains the same except for a subtle change in the definition of  $\tau_{ij}^p$ :

$$\tau_{ij}^{cr} = \frac{1}{1 - \frac{c_{kk}}{L^2}} (c_{ij} - \delta_{ij}). \quad (3.11)$$

From this, the FENE-MCR model is derived by making the approximation that  $Df/Dt \approx 0$ , where  $f = 1/(1 - c_{kk}/L^2)$ . Applying this simplification negates the need for defining a conformation tensor  $c_{ij}$  and allows for the direct solution of the polymer stress  $\tau_{ij}^{mcr}$ :

$$\frac{\partial \tau_{ij}^{mcr}}{\partial t} + u_k \frac{\partial \tau_{ij}^{mcr}}{\partial x_k} - \tau_{ik}^{mcr} \frac{\partial u_j}{\partial x_k} - \tau_{kj}^{mcr} \frac{\partial u_i}{\partial x_k} = \frac{g(\tau_{ij}^{mcr})}{Wi} \left( \frac{\partial u_i}{\partial x_j} + \frac{\partial u_j}{\partial x_i} - \tau_{ij}^{mcr} \right), \quad (3.12)$$

where

$$g(\tau_{ij}^{mcr}) = \frac{L^2 - Wi \tau_{kk}^{mcr}}{L^2 - 3} \quad (3.13)$$

For the cases that will be used for comparison, Oliveira (2001) used a polymer extensibility of  $L^2 = 100$  as well as a viscosity ratio of  $\beta = 0.9091$ .

Simulations were therefore performed using the same set of parameters not only for the FENE-P model (that was introduced earlier and will be utilized in the remainder of this study), but also using the FENE-MCR model used in Oliveira (2001) and described above. Among other quantities reported in table 4 of Oliveira (2001), the following measurements are compared to the current simulations:

(i) The vortex shedding frequency, defined as a dimensionless Strouhal number ( $St \equiv \Omega D/U_\infty$ , where  $\Omega$  is the shedding frequency).

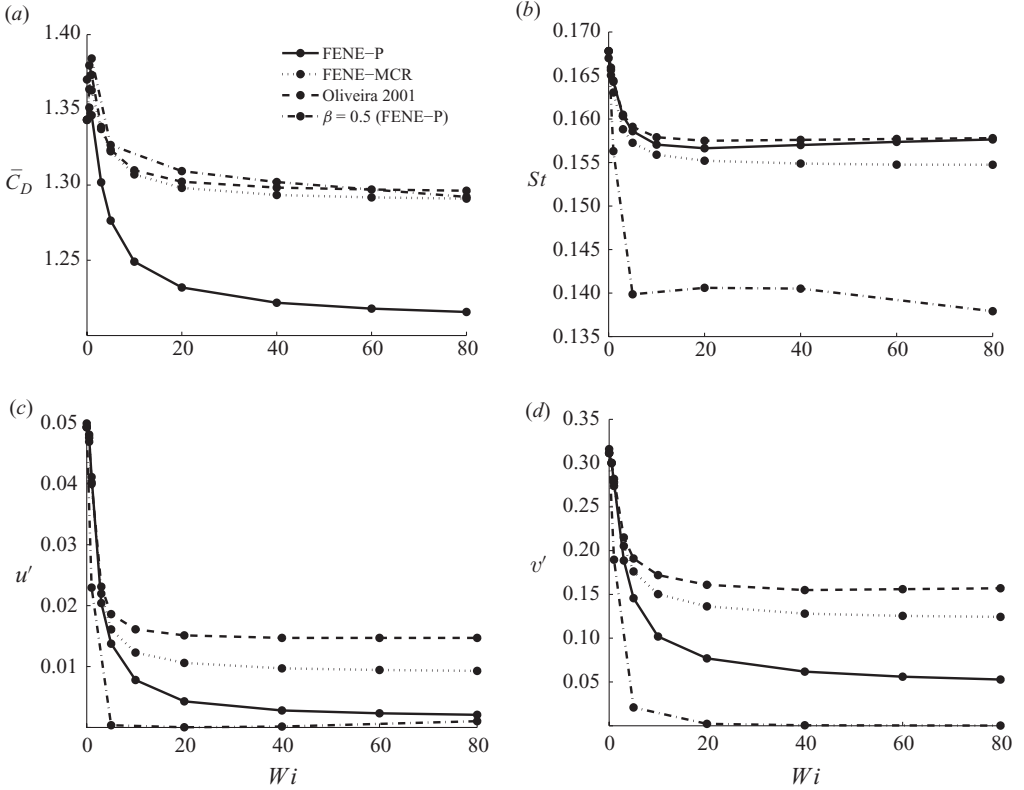


FIGURE 5. Comparisons of simulated data with that of Oliveira (2001): (a) average drag coefficient  $\bar{C}_D$ , (b) Strouhal number  $St$ , (c) streamwise root mean square (r.m.s.) velocity  $1D$  behind cylinder and (d) transverse r.m.s. velocity  $1D$  behind cylinder. Flow parameters are  $Re = 100$ ,  $L^2 = 100$  and  $\beta = 0.9091$ .

(ii) The total time-averaged drag on the cylinder,  $\bar{C}_D \equiv 1/2 (C_{D,max} + C_{D,min})$ .  $C_{D,max}$  and  $C_{D,min}$  indicate maxima and minima in time, respectively.

(iii) The r.m.s. transverse and streamwise velocities  $u'$  and  $v'$  along the  $y=0$  line at a  $x$  location of  $1D$  downstream of the cylinder

These comparisons are shown in figure 5. As can be seen in the plots, values from Oliveira (2001) and simulations performed with the FENE-MCR model show relatively good agreement for the drag and shedding frequency (each within 5%), but relative errors as large as 36% are seen for the velocity fluctuations at high  $Wi$ . This discrepancy likely has to do with the small magnitude of the velocity fluctuations compared to the mean values, thus making these quantities more susceptible to small numerical and round-off errors. Furthermore, data from the FENE-P simulations are qualitatively in agreement as well, in that they exhibit a reduction in vortex shedding frequency with increasing elasticity as well as a decrease in average drag and velocity fluctuations in the wake. The close agreement of the drag and frequency data, coupled with the convergence data which will be described shortly, provides sufficient confidence that the numerical method employed herein provides faithful results. Note that the FENE-MCR model has only been utilized here for comparison purposes, and that in all subsequent simulations only the FENE-P model will be used.

Quantity	Original mesh	Refined mesh	% Difference
$St$	0.1576	0.1574	0.127
$\bar{C}_D$	1.2157	1.2155	0.017
$\bar{C}_D^{pressure}$	0.9142	0.9138	0.044
$\bar{C}_D^{viscous}$	0.2614	0.2611	0.115
$\bar{C}_D^{polymer}$	0.0401	0.0407	1.49
$u'$	0.0021	0.002	4.76
$v'$	0.0528	0.0515	2.46

 TABLE 2. Mesh refinement results for  $Re = 100$ ,  $Wi = 10$ ,  $L^2 = 100$  and  $\beta = 0.9091$ .

In addition to comparing the current code to previous simulations, mesh refinement was also used to illustrate the grid independence of the solutions for the FENE-P calculations. First, for the case of two-dimensional laminar vortex shedding ( $Re = 100$ ), the same quantitative data that was compared to Oliveira (2001) was evaluated for two different mesh resolutions. Starting with Mesh 1, all grid cell lengths were consistently halved, thus making the test mesh twice as refined as the original. The quantities monitored during the mesh refinement consisted of the same data that was compared to Oliveira (2001) ( $St$ ,  $\bar{C}_D$ ,  $u'$  and  $v'$ ), as well as the individual components of the total drag resulting from pressure forces, viscous stresses and viscoelastic stresses, denoted  $\bar{C}_D^{pressure}$ ,  $\bar{C}_D^{viscous}$  and  $\bar{C}_D^{polymer}$ , respectively. These parameters were observed to be nearly unchanged, varying less than 5% for all quantities, as seen in table 2.

For the case of  $Re = 300$ , a slightly different mesh refinement procedure was used to illustrate the grid independence of the solutions obtained. Starting with Mesh 2 with a spanwise domain length of  $2\pi D$ , the number of grid points in the spanwise direction was increased until mean and average fluctuating velocity profiles in the cylinder wake converged, since for  $Re = 300$  the flow contains significant three-dimensional motions. The profiles of the streamwise velocity fluctuations  $u'$  are shown in figure 6. Other statistical quantities were also monitored (mean streamwise and transverse velocities and transverse velocity fluctuations), and similar convergence was attained. In the plots, the notation  $N32$  refers to 32 discretization points over the spanwise length of  $2\pi D$ ,  $N48$  to 48 points, etc. Noting that the profiles converge around 64 points, the mesh  $N64$  was used for all  $Re = 300$  results presented subsequently.

The combination of these validation tests illustrates that the viscoelastic code which has been developed is adequate for investigating a wide variety of unexplored problems, and interesting results from several different simulations will be presented in the following section.

## 4. Results and discussion

### 4.1. $Re = 100$

In Oliveira (2001) and in the previous section, it was shown that, in general, increased viscoelasticity produced a modest decrease in both the drag amplitude (defined  $\Delta C_D \equiv 1/2(C_{D,max} - C_{D,min})$ ) and the time-averaged drag,  $\bar{C}_D$ . Furthermore, the frequency of vortex shedding ( $St$ ) was also found to decrease simultaneously with a lengthening of the recirculation bubble immediately behind the cylinder. This, as was further discussed by Sahin & Owens (2004), is indicative of the stabilizing nature of viscoelasticity on the shear layer that develops as fluid flows over the cylinder surface. In fact, earlier work done by Azaiez & Homsy (1994a) on the linear stability

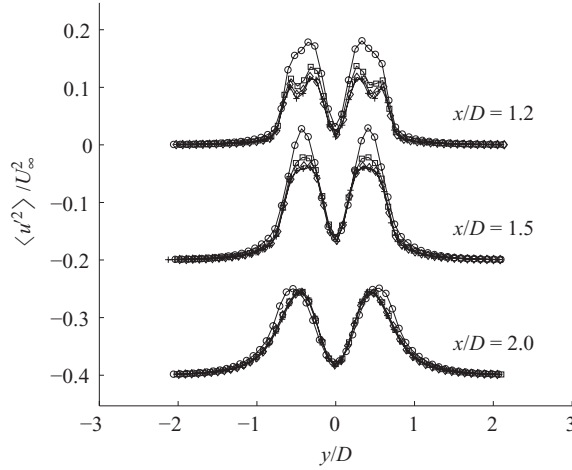


FIGURE 6. Spanwise mesh convergence plots for streamwise average fluctuating velocity profiles at multiple downstream stations. Simulations performed at  $Re = 300$ ,  $Wi = 10$ ,  $L^2 = 100$  and  $\beta = 0.9$ . ( $\circ$ )  $N30$ ; ( $\square$ )  $N48$ ; ( $+$ )  $N64$ ; ( $\diamond$ )  $N80$ .

of Oldroyd-B fluids has shown that shear instability growth rates are suppressed by the presence of viscoelasticity.

For many of the calculations performed by Oliveira (2001), a polymer extensibility of  $L^2 = 100$  was used, and the effect of  $L$  was tested up to a value of  $L^2 = 1200$ . In Sahin & Owens (2004), who also utilize the FENE-MCR model, values of  $L^2$  were no greater than 144 (note that in the limit  $L^2 \rightarrow \infty$  the family of FENE models approach the Hookean Oldroyd-B representation). As Oliveira (2001) points out, values of  $L^2 \sim O(100)$  can be appropriate for Boger fluids at high concentration, but for the types of flow motivating this study, much higher values are required. For example, in numerous recent studies done on turbulent drag reduction, typical values of  $L^2$  range of the order of 10 000 or above, which are required to reproduce experimentally observed values of the decrease in drag (Dimitropoulos *et al.* 2005; Dubief *et al.* 2005; Gupta *et al.* 2005; Dimitropoulos *et al.* 2006; Li *et al.* 2006). In these studies, the effect of viscoelasticity on the flow structure can be profound, therefore, for the case of two-dimensional vortex shedding at  $Re = 100$ , we chose to study the effect of high  $L$  in detail.

After setting  $L^2 = 10\,000$ ,  $Wi = 10$  and keeping the viscosity ratio  $\beta$  constant at 0.9, simulations revealed major qualitative changes to the cylinder wake structure as compared to the  $L^2 = 100$  and Newtonian cases. This is easily seen in the comparison of figure 7. In the figure, contours of the polymer stretch  $c_{kk}$  are shown, normalized with their maximum value within the domain. With the increase in polymer extensibility, there is a dramatic lengthening of the recirculation region behind the cylinder, closely resembling the different downstream behaviour of polymer additives WSR 301 and WSR 303 as shown experimentally by Cadot & Lebey (1998). Measuring the length of the recirculation bubble  $l$  as the distance between the rear stagnation point of the cylinder and the point where the maximum transverse velocity fluctuation occurs, this distance increases from  $l = 4.18D$  to  $l = 5.16D$ .

Although Cadot & Lebey (1998) cite a difference in elasticity number ( $E \equiv Wi/Re = \lambda v/\delta^2$ , where  $\lambda$  is the polymer relaxation time,  $v$  the fluid viscosity and  $\delta$  the shear layer thickness) as the cause of the further lengthening of the

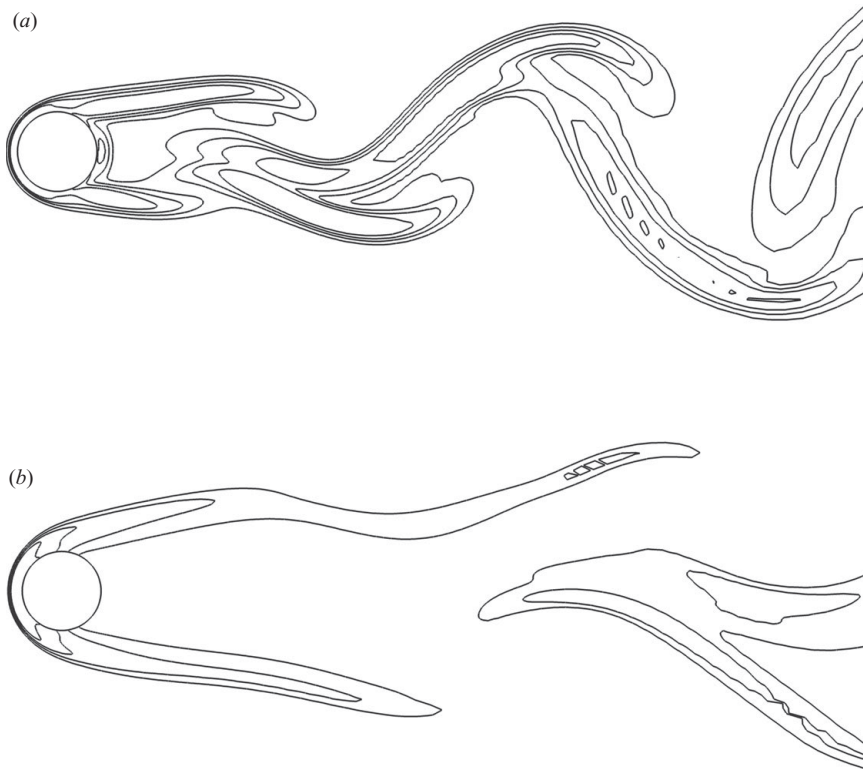


FIGURE 7. Comparison of vortex shedding pattern between  $L^2 = 100$  and  $L^2 = 10\,000$ . Contours are of normalized trace  $c_{kk}/\max(c_{kk})$ . Levels include  $c_{kk}/\max(c_{kk}) = 0.2, 0.4, 0.6, 0.8$  and  $1.0$ . Maximum  $c_{kk}$  for each case are (a)  $\max(c_{kk}) = 97.39$ , (b)  $\max(c_{kk}) = 7904$ . Simulations performed at  $Re = 100$ ,  $Wi = 10$  and  $\beta = 0.9$ .

recirculation region when using WSR 303 versus WSR 301, figure 7 suggests that extensional properties, namely extensional viscosity, must play a role in the delay of shear layer instabilities since in both cases the Weissenberg number is held constant. This is consistent with the conclusions of the previous experimental work of Cressman *et al.* (2001) and computational work of Sahin & Owens (2004).

Furthermore, in an effort to determine whether or not this lengthening of the wake is a result of a transient value or a plateau value of the extensional viscosity, the total strain experienced by a polymer was computed along several streamlines which travel through the shear layer. By projecting the local strain rate onto the local polymer orientation (easily computed from the conformation  $c_{ij}$ ), it was found that after integrating up to the point where a vortex was being shed, the total strain felt by a dumbbell residing in the shear layer was roughly  $\epsilon \approx 4$ . Based on numerous experimental studies, this amount of strain is not adequate for a steady extensional viscosity to form before the polymer is entrained into a developing vortex (see McKinley & Sridhar 2002). Therefore, we conclude that this effect is due to a transient value of the extensional viscosity.

Perhaps more remarkable than the increase in the recirculation region is the response of the cylinder drag due to the increase in polymer extensibility. As we recall from figure 5, when holding the extensibility  $L^2$  constant at 100, the average drag reduced by approximately 9% when increasing  $Wi$  from 0 to 80. This behaviour has

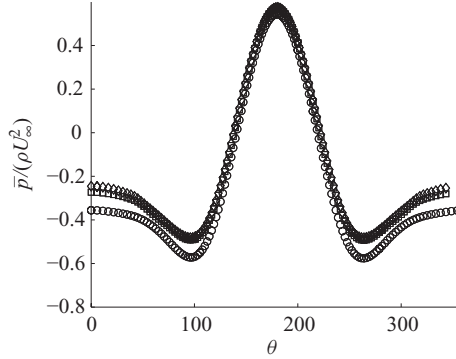


FIGURE 8. Dimensionless pressure distribution over cylinder for Newtonian flow and for  $L^2 = 100$  with varying  $Wi$ . ( $\circ$ ) Newtonian; ( $\square$ )  $Wi = 10$ ; ( $\diamond$ )  $Wi = 80$ . Polar angle  $\theta$  measured counter-clockwise from rear stagnation point.  $Re = 100$  and  $\beta = 0.9$  for all simulations.

been seen experimentally by Coelho & Pinho (2004), who see a form drag decrease for dilute solutions of tylose and CMC at  $Re < 800$ , and Kato & Mizuno (1983), who observe similar behaviour for dilute PEO solutions. This decrease is said to result from a rising base pressure on the back side of the cylinder, which is required to maintain an equilibrium of forces on the recirculation bubble due to a decrease in shear stresses (Coelho & Pinho 2004). A rise in the back pressure is in fact seen experimentally in both studies, which, integrated over the surface of the cylinder, results in a diminished form drag. In the present simulations, the base pressure for the case of low polymer extensibility exhibited this same behaviour, as seen in figure 8 where the time-averaged pressure distribution over the cylinder is plotted.

For larger polymer extensibilities, however, the drag actually increases when compared to the Newtonian value at a constant  $Wi$ . At  $Wi = 10$  and  $L^2 = 10\,000$ , the average drag coefficient takes on a value of  $\bar{C}_D = 2.7$ , compared to the  $L^2 = 100$  value of 1.25 and the Newtonian value of 1.34. This dramatic drag increase has also been seen experimentally by James & Gupta (1971), who observed a similar substantial increase in drag for different polymer solutions with different blends of polyox WSR (not the same used by Cadot & Lebey 1998). To explain the striking difference between this case and that of lower polymer extensibility, the time-averaged surface pressure distribution for increasingly high  $L$  is shown in figure 9. Comparing this to figure 8, it is immediately obvious that the jump in drag is due to the significantly changed pressure distribution on the cylinder. Although there is still a modest increase in the back pressure, the high extensibility case is dominated instead by a near threefold increase in the forward stagnation point pressure as  $L^2$  is increased towards a value of 22 500. It has been speculated that the cause of this effect results from the solid-like behaviour of the viscoelastic fluid (see Coelho & Pinho 2004; Metzner & Astarita 1967).

To explain this effect, the plots of figure 10 show the velocity, pressure and polymer fractional extension along the upstream stagnation streamline (the cylinder surface is located at  $x/D = -0.5$ ). Note that the same profiles for Newtonian flow are not included since they are quantitatively similar to that of the  $Wi = 10$ ,  $L^2 = 100$  case (shown with solid lines). As a fluid element traverses the forward stagnation streamline, it eventually reaches a point where it begins to behave as if it were approaching a solid wall. For the  $L^2 = 100$  case, this point is nearly located on the cylinder surface ( $x/D \approx -0.55$ ), while for the high extensibility case, this point is offset to a point

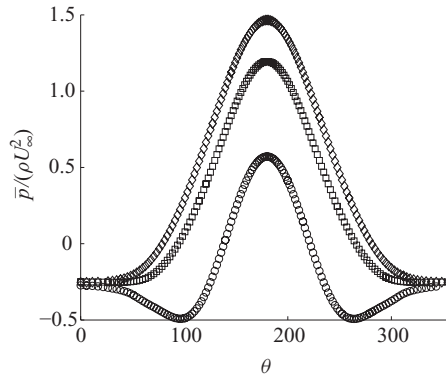


FIGURE 9. Dimensionless pressure distribution over cylinder at  $Wi = 10$  and increasing  $L$ . ( $\circ$ )  $L^2 = 100$ ; ( $\square$ )  $L^2 = 10\,000$ ; ( $\diamond$ )  $L^2 = 22\,500$ . Polar angle  $\theta$  measured counter-clockwise from rear stagnation point.  $Re = 100$  and  $\beta = 0.9$  for all simulations.

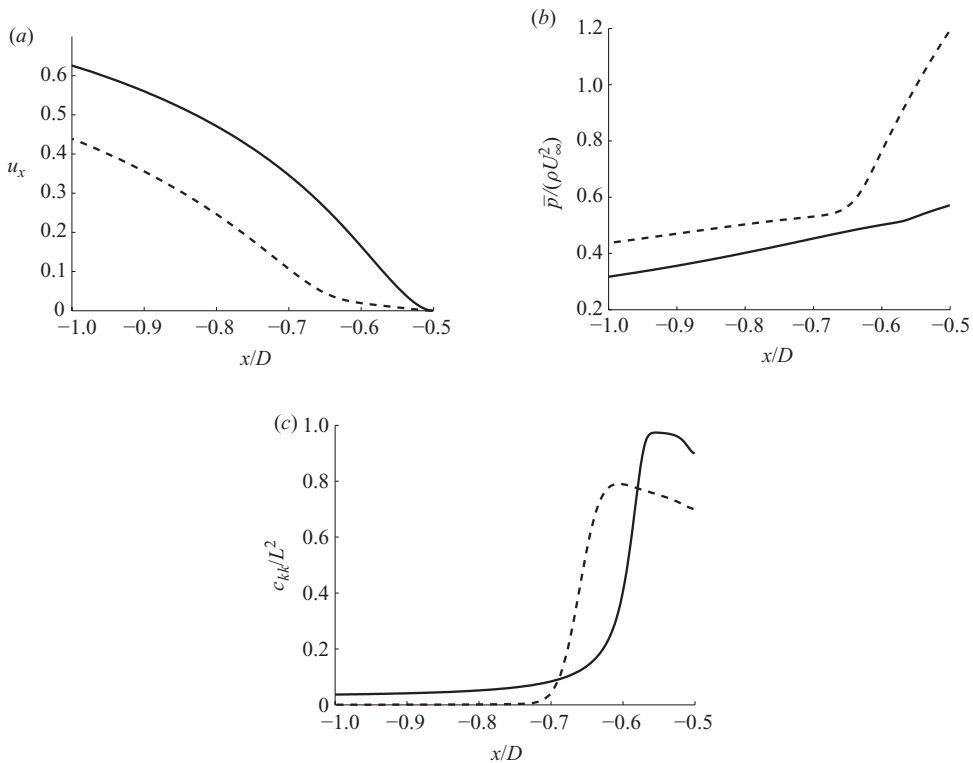


FIGURE 10. Computed values of (a) streamwise velocity  $u_x$ , (b) dimensionless pressure  $\bar{p}/(\rho U_\infty^2)$  and (c) polymer fractional extension  $c_{kk}/L^2$  along the stagnation streamline. (—)  $Wi = 10$ ,  $L^2 = 100$ ; (---)  $Wi = 10$ ,  $L^2 = 10\,000$ . Cylinder forward stagnation point begins at  $x/D = -0.5$ .  $Re = 100$  and  $\beta = 0.9$  for all simulations.

slightly upstream:  $x/D \approx -0.65$ . At these locations, a sharp increase in the polymer stretch (figure 10c) coincides with a decrease to a near-zero velocity (figure 10a) and a rise in pressure to its Bernoulli-type stagnation value of  $\bar{p} = 0.5$  (figure 10b). Note that beyond the offset stagnation point of  $x/D \approx -0.65$ , the pressure for the

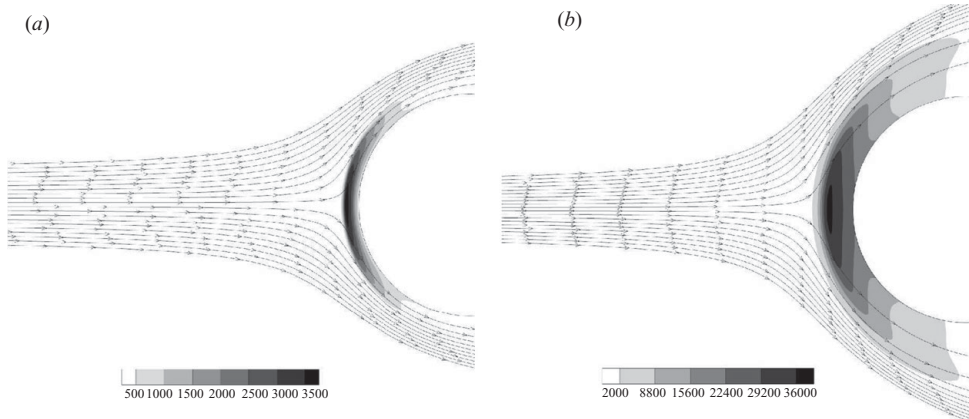


FIGURE 11. Upstream velocity streamlines showing the ‘offset’ stagnation point due to high polymeric stress. (a)  $Wi = 10$ ,  $L^2 = 100$ ; (b)  $Wi = 10$ ,  $L^2 = 10000$ . Contours are of  $\tau_{22}^p$  with values shown in legend.  $Re = 100$  and  $\beta = 0.9$  for both simulations.

$L^2 = 10000$  case rises dramatically above this value due to the high polymer stresses near the cylinder surface.

According to the work done by Metzner & Astarita (1967), an appropriate measure of the solid-like response of viscoelastic fluids near stagnation point flow is a local Deborah number based on the material rate of change of the strain rate:  $De_{local} = \lambda \sqrt{|D\Gamma/Dt|}$ , where, as before,  $\lambda$  is a characteristic polymer relaxation time and  $\Gamma$  is the second invariant of the local strain rate tensor. This dimensionless parameter provides a ratio of the polymer relaxation time scale to the flow time scale based on the local deformation rate; thus, for high  $De_{local}$ , fluid strain occurs on time scales smaller than the stress relaxation time of the polymer, resulting in a solid-like response of the viscoelastic fluid. When computing these values, a peak in  $De_{local}$  which is several times the magnitude of the flow Weissenberg number is found to occur in the same locations: a peak of  $De_{local} = 36.7$  at  $x/D \approx -0.55$  for the low extensibility case and a peak of  $De_{local} = 21.2$  at  $x/D \approx -0.65$  for the high extensibility case.

Finally, figure 11 further illustrates this offset stagnation point by showing contours of polymer stress  $\tau_{22}^p$  with velocity streamlines overlaid. For  $Wi = 10$  and  $L^2 = 100$  (figure 11a), only modest polymeric stresses develop, and thus the streamlines are not altered significantly from their Newtonian counterpart (not shown). However, for the  $Wi = 10$ ,  $L^2 = 10000$  case (figure 11b), the polymer stresses are roughly an order of magnitude larger, which causes the upstream flow to be diverted at the same respective locations mentioned previously. Comparing figure 11(b) with figure 1 of Metzner & Astarita (1967) clearly corroborates their discussion of a solid-like stagnation point boundary.

As a final note for the  $Re = 100$  case, the effects of shear thinning and polymer concentration were briefly investigated. As reported by Coelho & Pinho (2003b), the effect of shear thinning on viscoelastic cylinder flow is to increase the vortex shedding frequency, while fluid elasticity tends to decrease it. Therefore, since the FENE-P model exhibits shear thinning behaviour through the extra polymer stress  $\tau_{ij}^p$ , additional simulations were performed at  $\beta = 0.5$  (rather than  $\beta = 0.9$ ) in order to probe the effect of increasing the shear thinning contribution to the total viscosity.

At this value of the viscosity ratio, the value of  $St$  at Weissenberg numbers ranging from 0 to 80 were seen to actually decrease further from the Newtonian value than the previous  $\beta = 0.9$  results, while the drag increased (seen in figure 5). This is qualitatively the same behaviour as when the polymer extensibility was increased from  $L^2 = 100$  to  $L^2 = 10\,000$ . Furthermore, contours of polymer stretch and velocity in the cylinder wake (not shown) revealed similar characteristics to the high polymer extensibility case seen in figure 7(b). This is entirely consistent with the experimental findings of Coelho & Pinho (2003b) since as  $\beta$  is decreased, the decreased shear viscosity is accompanied by an increased extensional viscosity. Therefore, although the FENE-P fluid is shear thinning, lowering the viscosity ratio  $\beta$  results in a competing increase in the extensional viscosity which causes the same rise in drag, decrease in  $St$ , and lengthening in the wake as seen when increasing the polymer extensibility  $L$ . Moreover, this behaviour is further corroborated by experiments done by Usui *et al.* (1980), who note a decrease in vortex shedding frequency whose magnitude increases with increasing polymer concentration. Again this is entirely consistent with the present results since the parameter  $\beta$  effectively controls the polymer concentration.

#### 4.2. $Re = 300$

At a value of  $Re = 300$ , Newtonian flow past a cylinder is located in the so-called wake transition regime, where three-dimensional structures begin to form in the wake as transition takes place from the purely laminar two-dimensional case (Williamson 1996b; Zdravkovich 1997). This regime is demarcated by a Reynolds number at which a sharp, hysteretic drop in the shedding frequency is observed and inception of spanwise instabilities occurs, termed mode ‘A’ instabilities by Williamson (1996a). These mode A instabilities are a result of vortex loops that form and stretch into streamwise vortex pairs and have a spanwise wavelength of  $\sim 3.5D$ . With further increase in the Reynolds number, mode A instabilities give way to a new mode of spanwise instability, referred to as mode ‘B’ instabilities. The mode B instabilities are smaller in scale compared to the mode A counterpart, and appear as counter-rotating streamwise vortices immediately downstream of the cylinder with a wavelength of  $\sim 1D$ . As with the mode A instabilities, the mode B vortices are indicative of three-dimensional transition in Newtonian flow, but they are present until the entire shear layer breaks down to full turbulence.

To evaluate the effect of viscoelasticity on the formation of three-dimensional wake instabilities, simulations were first performed at  $Re = 300$  with  $L^2 = 100$ ,  $Wi = 10$  and  $\beta = 0.9$ . At this Reynolds number, mode B instabilities should dominate the spanwise structure (rather than mode A) for a Newtonian fluid (see Williamson 1996a). From the isosurfaces of streamwise vorticity ( $\omega_x = \pm 0.5$ ) compared in figure 12, it is clear that viscoelasticity suppresses the formation of these mode B instabilities. Instead of exhibiting their highly regular alternating pattern as in the Newtonian case, the streamwise vortices that form are fewer in number across the span of the domain in the presence of viscoelasticity. In fact, the spanwise wavelength of the streamwise vortices in the Newtonian case is  $\lambda \approx 0.93D$ , agreeing with experiments of Williamson (1996a), while that of the viscoelastic case increases threefold:  $\lambda \approx 3.30D$ .

One interesting point to note is that the characteristic wavelength of the mode A instabilities for a Newtonian fluid is  $\lambda \approx 3D$  at this Reynolds number, so at first glance it may appear that viscoelasticity is merely delaying the onset of the Newtonian modes of three-dimensional transition. Corroborating this conjecture, the symmetries of the vortices found in figures 12(a) and 12(b) are found to agree with those of mode B and mode A instabilities, respectively. As described in detail in Williamson

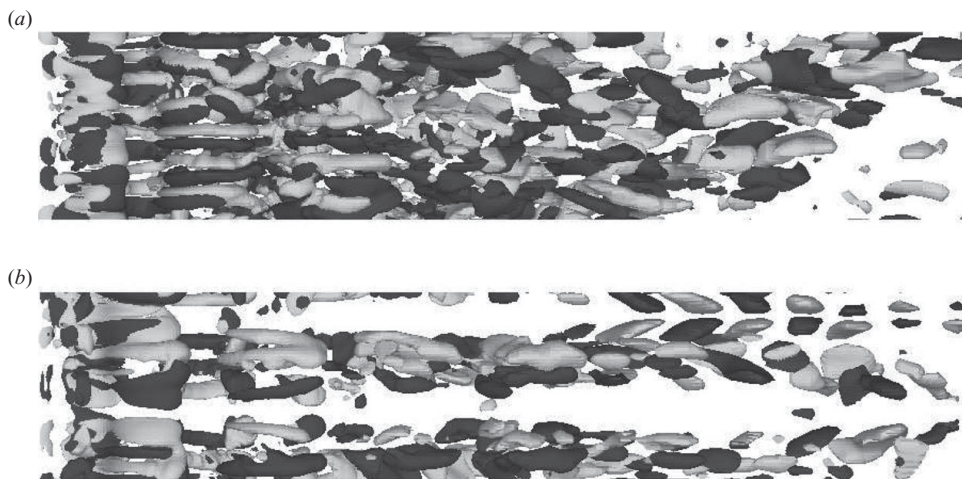


FIGURE 12. Comparison of streamwise vorticity isosurfaces ( $\omega_x = \pm 0.5$ ) in  $Re = 300$  flow. (a) Newtonian; (b)  $Wi = 10$ ,  $L^2 = 100$  and  $\beta = 0.9$ .

(1996a), mode A instabilities exhibit opposite signs of rotation on either side of a primary spanwise vortex, while mode B instabilities maintain the same sign through the primary spanwise vortices. This pattern can be seen in the current simulations by inspecting the signs of vorticity in the contours of figure 12 and following one vortex filament in the downstream direction.

In order to verify that this modified vortex structure is genuine and not a consequence of the spanwise domain size, the same simulation was performed on a grid whose span was doubled (from  $2\pi D$  to  $4\pi D$ ) and both the structure and wavelength were found to remain the same.

As in the case of  $Re = 100$ , the effect of raising the polymer extensibility from  $L^2 = 100$  to a length of  $L^2 = 10000$  is significant. Isosurfaces of polymer fractional extension ( $c_{kk}/L^2$ ) are presented in figure 13, and the most striking effect of the high extensibility is the complete suppression of all three-dimensional structure. All streamwise vorticity is inhibited, and the two-dimensional wake profile looks qualitatively similar to that of the  $Re = 100$ ,  $L^2 = 10000$ ,  $Wi = 10$  case. Thus, one important point to keep in mind is that if figure 12 included the results from the high extensibility case, or equivalently if figure 13 were plotted with streamwise vorticity isosurfaces, nothing would appear.

The experiments of Cadot & Kumar (2000) observed this same effect by injecting high-molecular-weight Polyox WSR 303 into flows at slightly lower Reynolds numbers. At  $Re = 190$ , a Reynolds number which exhibits the longer wavelength mode A instabilities in the Newtonian case, Cadot & Kumar (2000) see a near complete suppression of all spanwise variation at adequately high polymer concentration. Citing previous numerical work on the roll-up instabilities of a FENE-P fluid (Kumar & Homsy 1999), they speculate that this suppression of three-dimensional instability growth is due to a modification of the spanwise vortices that develop rather than a purely three-dimensional effect.

To illustrate that this truly is the physical mechanism responsible for this three-dimensional instability suppression, figure 14 shows instantaneous contours of spanwise vorticity in the  $x$ - $y$  planes (at  $z/D = 3.14$ ) for both  $L^2 = 100$  and  $L^2 = 10000$ . Dark contours indicate a value of  $\omega_z = -1.5$  and white contours indicate  $\omega_z = +1.5$ .

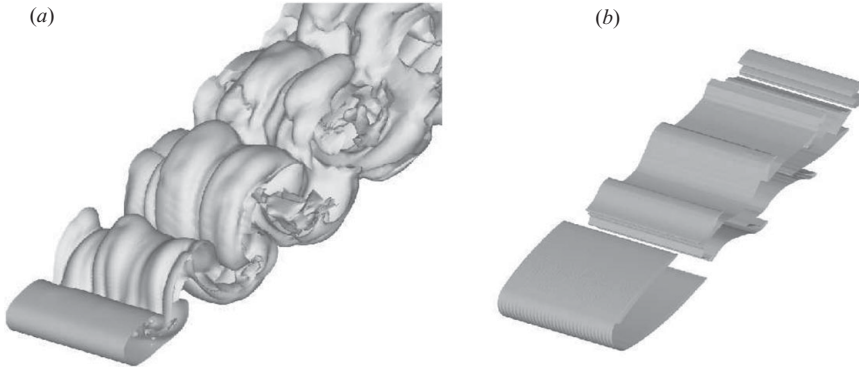


FIGURE 13. Isosurfaces of 25 % fractional extension ( $c_{kk}/L^2=0.25$ ) showing suppression of three-dimensional structures with high polymer extensibility. (a)  $Re = 300$ ,  $Wi = 10$ ,  $L^2 = 100$ ,  $\beta = 0.9$ ; (b)  $Re = 300$ ,  $Wi = 10$ ,  $L^2 = 10\,000$ ,  $\beta = 0.9$ .

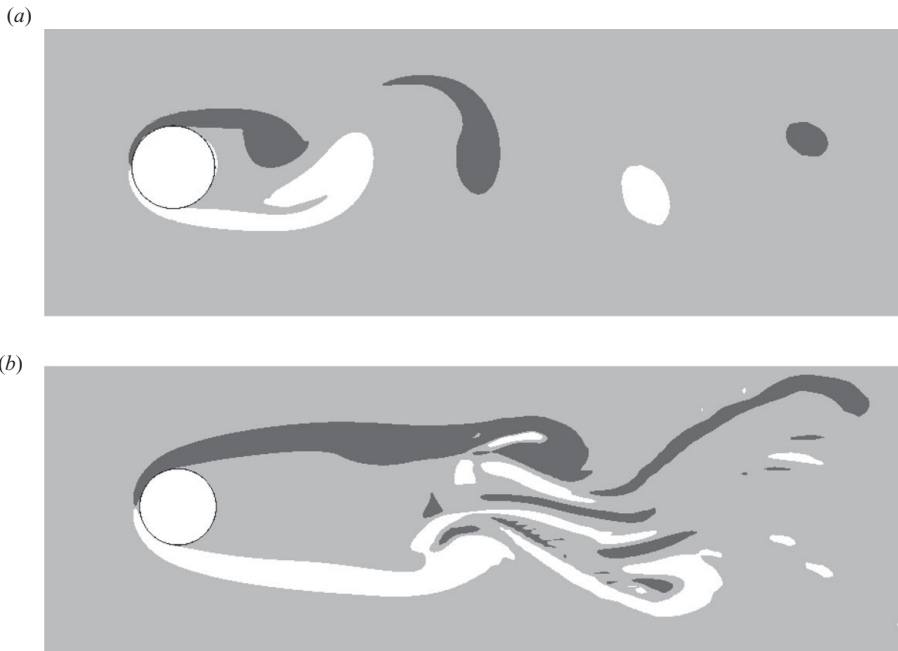


FIGURE 14. Contours of spanwise vorticity in a plane located at  $z/D = 3.14$ . Dark colouring indicates  $\omega_z = -1.5$  and light colouring indicates  $\omega_z = +1.5$ . (a)  $Re = 300$ ,  $Wi = 10$ ,  $L^2 = 100$ ,  $\beta = 0.9$ ; (b)  $Re = 300$ ,  $Wi = 10$ ,  $L^2 = 10\,000$ ,  $\beta = 0.9$ .

In the case of  $L^2 = 100$  (figure 14a), the primary vortex roll-up process looks very similar to that of Newtonian flow. Here, large regions of positive spanwise vorticity are generated from the lower shear layer and regions of negative spanwise vorticity are generated in the upper shear layer, as expected. In general, coherent structures of like-signed vorticity do not mix with vorticity of opposite sign, and the highest magnitude vorticity (in the wake) is found in the centre of each primary vortex.

For higher polymer extensibility, however, shown in figure 14(b), small regions of opposite signed vorticity are generated near the core of each primary vortex, greatly inhibiting its formation. In their study of a time-developing shear layer, Kumar &

Homsy (1999) observe similar behaviour. They found that during the two-dimensional roll-up process, contributions from the elastic source term in the vorticity transport equation prevented the spanwise vorticity to concentrate into a single core, thus resisting the two-dimensional roll-up. Kumar & Homsey (1999) then show that this interference with two-dimensional roll-up is a much more effective mechanism for suppressing the growth of three-dimensional instabilities than elasticity merely slowing the growth from an already-developed two-dimensional base state. In other words, for cases where the primary vortex roll-up is unaffected, stabilization to three-dimensional instabilities is weakened relative to the case where the primary vortex sheet is greatly distorted. Comparing these results to the current simulations, we see that exactly the same mechanism is manifesting itself in the cylinder wake. For the case of  $Wi = 10$ ,  $L^2 = 100$ , the two-dimensional primary vortex roll-up is relatively unaffected by the presence of viscoelasticity (seen in figure 14a), and as a result, the resistance of the flow to the three-dimensional mode B instabilities is modest (figure 12b). In the case of  $Wi = 10$ ,  $L^2 = 10\,000$ , significant distortion of the primary vortex street is observed (figure 14b), thus completely stabilizing the growth of all three-dimensional structures (figure 13b).

## 5. Conclusions

By modifying an existing incompressible Navier–Stokes flow solver created at Stanford University, a code was developed that was used to perform a detailed investigation of the physical effects that viscoelasticity has on a canonical bluff body flow. After validating the accuracy of the code through a series of test cases, simulations were performed at two distinct Reynolds numbers:  $Re = 100$  and  $Re = 300$ . For the former, results were first compared to existing simulations at the same  $Re$  as completed by Oliveira (2001). For modest values of the polymer extensibility ( $L^2 = 100$ ), the same effects seen in Oliveira (2001) were observed; namely, a slight reduction in the vortex shedding frequency, a reduction in the time-averaged drag (as well as all individual components of the drag), a lengthening of the recirculation region behind the cylinder, and a dampening of velocity fluctuations in the wake. However, upon increasing the polymer extensibility ( $L^2 = 10\,000$ ), significant qualitative changes to the cylinder wake were discovered. In this case, the time-averaged drag sharply increased with increasing polymer extensibility due to a solid-like behaviour of the polymer stress on the forward stagnation point. As with the effects at low polymer extensibility, this is an effect which had previously been seen experimentally.

For the case of  $Re = 300$ , results focused on the ability of the viscoelasticity to stabilize the flow to three-dimensional instabilities. For Newtonian flow at this Reynolds number, mode B instabilities dominate the near-wake structure, but when polymer additives are introduced, the characteristic spanwise vortices undergo significant alterations. For low polymer extensibilities ( $L^2 = 100$ ), the spanwise vortex wavelength increases from roughly  $1D$  towards  $3D$  (one more closely resembling that of mode A instabilities). This, coupled with the fact that the streamwise vortex symmetry also appears to resemble that of mode A instabilities hints of a stabilization mechanism which merely delays the Newtonian modes of instability. Without further evidence, this result cannot be stated conclusively and thus it provides a very interesting topic of future work. Flows with a high polymer extensibility ( $L^2 = 10\,000$ ), however, exhibit a total suppression of all three-dimensional instability growth. Like the suppression of mode A instabilities seen by Cadot & Kumar (2000), a high polymer extensibility appears to suppress the formation of mode B instabilities. The

mechanism behind this suppression was drawn from that of Kumar & Homsy (1999) and is primarily due to an inhibition of the formation of the primary spanwise vortices.

Finally, because one of the primary goals of this study was to extend the understanding gained from existing turbulent drag reduction studies, it seems prudent to relate the current findings to the underlying drag reduction mechanisms which have been previously discovered. Specifically, the recent work done by Stone *et al.* (2004) and Kim *et al.* (2007) clearly illustrate the importance of streamwise vorticity dampening within the turbulent buffer layer to achieve reductions in near-wall Reynolds stresses and thus reduced drag. By examining the interaction of viscoelasticity with exact coherent states (ECS) found in plane Couette flow, Stone *et al.* (2004) showed that for moderately low Reynolds numbers, streamwise vortical structures which dominate the Newtonian solution are weakened by the presence of viscoelastic stresses. This causes both a redistribution near-wall velocity fluctuations, and stabilizes the flow (seen by an upward shift in the minimum Reynolds number required for a drag-reduced ECS solution to exist). To extend this description, Kim *et al.* (2007) use conditional eddies from direct numerical simulation data to illustrate the mechanistically simple explanation of viscoelastic torques which are found acting against the near-wall streamwise vortices in drag-reduced high-Reynolds-number channel flow. Again, they report that this effect is at least partially the cause of dampening of Reynolds shear stress production and thus contributes to overall drag reduction.

Therefore, the mode B instability suppression found in the present study can now be seen in a different light. Although the shear layers developed in the wake of a cylinder are not entirely analogous to the plane shear flow of Stone *et al.* (2004), the dampening of streamwise vortical structures in the cylinder wake obviously has certain implications for the near-wall vortices of turbulent channel flow. As pointed out by Cadot & Kumar (2000) after experimentally observing a dampening of mode A instabilities, the stabilization of Kelvin–Helmholtz type instabilities is one method through which viscoelasticity can inhibit vorticity filament formation in turbulent flows. Since such an inflectional instability is one step in the self-sustaining process of ECS structures of Stone *et al.* (2004), and since the existence of the ECS presumably precedes transition to turbulence, the mechanisms seen in the present study for delaying the onset of primary roll-up instabilities formed in the wake can be related to mechanisms through which polymer additives can reduce skin friction drag. Furthermore, the concept of weakening near-wall vortices through viscoelastic torques described by Kim *et al.* (2007) could possibly be applied to the present case, since preliminary evidence suggests that these torques do exist in the wake immediately behind the cylinder (not shown here). Thus, the mechanisms behind drag reduction and the mode B instability suppression may have a partially common explanation.

The authors would like to acknowledge the Army High Performance Computing Research centre for Agility, Survivability and Informatics, Award No. W911NF-07-2-0027, High Performance Technologies Inc and Department of the Army (Prime) for partial financial and computational support. In addition, this research has been funded in part by a King Abdullah University of Science and Technology (KAUST) research grant under the KAUST Stanford Academic Excellence Alliance program. Any opinions, findings and conclusions or recommendations expressed in this paper are those of the authors and do not necessarily reflect the views of the KAUST University.

## REFERENCES

- AZAIIEZ, J. & HOMSY, G. 1994a Linear stability of free shear flow of viscoelastic liquids. *J. Fluid Mech.* **268**, 37–69.
- AZAIIEZ, J. & HOMSY, G. 1994b Numerical simulation of non-newtonian free shear flows at high Reynolds numbers. *J. Non-Newton. Fluid Mech.* **52**, 333–374.
- BIRD, R. B., ARMSTRONG, R. C. & HASSAGER, O. 1987 *Dynamics of Polymeric Liquids, Volume 1*, 2nd edn. Wiley.
- BIRD, R. & WIEST, J. 1995 Constitutive equations for polymeric liquids. *Annu. Rev. Fluid Mech.* **27**, 167–193.
- BROADBENT, M. & MENA, B. 1974 Slow flow of an elastico-viscous fluid past cylinders and spheres. *Chem. Engng J.* **8**, 11–19.
- CADOT, O. & KUMAR, S. 2000 Experimental characterization of viscoelastic effects on two- and three-dimensional shear instabilities. *J. Fluid Mech.* **416**, 151–172.
- CADOT, O. & LEBEY, M. 1998 Shear instability inhibition in a cylinder wake by local injection of a viscoelastic fluid. *Phys. Fluids* **11** (2), 494–496.
- CHILCOTT, M. & RALLISON, J. 1998 Creeping flow of dilute polymer solutions past cylinders and spheres. *J. Non-Newton. Fluid Mech.* **1988**, 381–432.
- COATES, P., ARMSTRONG, R. & BROWN, R. 1992 Calculation of steady-state viscoelastic flow through axisymmetric contractions with the eeme formulation. *J. Non-Newton. Fluid Mech.* **42**, 141–188.
- COELHO, P. & PINHO, F. 2003a Vortex shedding in cylinder flow of shear-thinning fluids. I. Identification and demarcation of flow regimes. *J. Non-Newton. Fluid Mech.* **110**, 143–176.
- COELHO, P. & PINHO, F. 2003b Vortex shedding in cylinder flow of shear-thinning fluids. II. Flow characteristics. *J. Non-Newton. Fluid Mech.* **110**, 177–193.
- COELHO, P. M. & PINHO, F. T. 2004 Vortex shedding in cylinder flow of shear-thinning fluids. III. pressure measurements. *J. Non-Newton. Fluid Mech.* **121**, 55–68.
- CRESSMAN, J. R., BAILEY, Q. & GOLDBURG, W. I. 2001 Modification of a vortex street by a polymer additive. *Phy. Fluids* **13** (4), 867–871.
- CRUZ, D. O. A., PINHO, F. T. & OLIVEIRA, P. J. 2005 Analytical solutions for fully developed laminar flow of some viscoelastic liquids with a newtonian solvent contribution. *J. Non-Newton. Fluid Mech.* **132**, 28–35.
- DIMITROPOULOS, C. D., DUBIEF, Y., SHAQFEH, E. S. G. & MOIN, P. 2006 Direct numerical simulation of polymer-induced drag reduction in turbulent boundary layer flow of inhomogeneous polymer solutions. *J. Fluid Mech.* **566**, 153–162.
- DIMITROPOULOS, C. D., DUBIEF, Y., SHAQFEH, E. S. G., MOIN, P. & LELE, S. K. 2005 Direct numerical simulation of polymer-induced drag reduction in turbulent boundary layer flow. *Phys. Fluids* **17** (1), 011705.
- DIMITROPOULOS, C., SURESHKUMAR, R. & BERIS, A. 1998 Direct numerical simulation of viscoelastic turbulent channel flow exhibiting drag reduction: effect of the variation of rheological parameters. *J. Non-Newton. Fluid Mech.* **79**, 433–468.
- DUBIEF, Y., TERRAPON, V. E., WHITE, C. M., SHAQFEH, E. S. G., MOIN, P. & LELE, S. K. 2005 New answers on the interaction between polymers and vortices in turbulent flows. *Flow Turbul. Combust.* **74** (4), 311–329.
- DUBIEF, Y., WHITE, C. M., TERRAPON, V. E., SHAQFEH, E. S. G., MOIN, P. & LELE, S. K. 2004 On the coherent drag-reducing and turbulence-enhancing behaviour of polymers in wall flows. *J. Fluid Mech.* **514**, 271–280.
- FAN, Y., TANNER, R. & PHAN-THIEN, N. 1999 Galerkin/least-square finite-element methods for steady viscoelastic flows. *J. Non-Newton. Fluid Mech.* **84**, 233–256.
- GADD, G. 1966 Effects of long-chain molecule additives in water on vortex streets. *Nature* **211**, 169–170.
- GUPTA, V., SURESHKUMAR, R. & KHOMAMI, B. 2005 Passive scalar transport in polymer drag-reduced turbulent channel flow. *AIChE J.* **51** (7), 1938–1950.
- HAM, F. & IACCARINO, G. 2004 Energy conservation in collocated discretization schemes on unstructured meshes. In *CTR Annual Research Briefs*, pp. 3–14.
- HAM, F., MATTSSON, K. & IACCARINO, G. 2006 Accurate and stable finite volume operators for unstructured flow solvers. In *CTR Annual Research Briefs*, pp. 243–261.

- JAMES, D. & GUPTA, O. 1971 Drag on circular cylinders in dilute polymer solutions. *Chem. Engng Prog. Symp. Ser.* **67** (111), 62–73.
- KALASHNIKOV, V. & KUDIN, A. 1970 Kármán vortices in the flow of drag-reducing polymer solutions. *Nature* **225**, 445–446.
- KATO, H. & MIZUNO, Y. 1983 An experimental investigation of viscoelastic flow past a circular cylinder. *Bull. Japan Soc. Mech. Eng.* **26** (214), 529–536.
- KIM, K., LI, C., SURESHKUMAR, R., BALACHANDAR, S. & ADRIAN, R. 2007 Effects of polymer stresses on eddy structures in drag-reduced turbulent channel flow. *J. Fluid Mech.* **584**, 281–299.
- KUMAR, S. & HOMSY, G. 1999 Direct numerical simulation of hydrodynamic instabilities in two- and three-dimensional viscoelastic free shear layers. *J. Non-Newton. Fluid Mech.* **83**, 249–276.
- LI, C., SURESHKUMAR, R. & KHOMAMI, B. 2006 Influence of rheological parameters on polymer induced turbulent drag reduction. *J. Non-Newton. Fluid Mech.* **140**, 23–40.
- LIU, A., BORNSIDE, D., ARMSTRONG, R. & BROWN, R. 1998 Viscoelastic flow of polymer solutions around a periodic, linear array of cylinders: comparisons of predictions for microstructure and flow fields. *J. Non-Newton. Fluid Mech.* **77**, 153–190.
- MA, X., SYMEONIDIS, V. & KARNIADAKIS, G. 2003 A spectral vanishing viscosity method for stabilizing viscoelastic flows. *J. Non-Newton. Fluid Mech.* **115**, 125–155.
- MAHESH, K., CONSTANTINESCU, G. & MOIN, P. 2004 A numerical method for large-eddy simulation in complex geometries. *J. Comput. Phys.* **197**, 215–240.
- MANERO, O. & MENA, B. 1981 On the slow flow of viscoelastic fluids past a circular cylinder. *J. Non-Newton. Fluid Mech.* **9**, 379–387.
- MCKINLEY, G., ARMSTRONG, R. & BROWN, R. 1993 The wake instability in viscoelastic flow past confined circular cylinders. *Phil. Trans. R. Soc. Lond.* **344** (1671), 265–304.
- MCKINLEY, G. & SRIDHAR, T. 2002 Filament-stretching rheometry of complex fluids. *Annu. Rev. Fluid Mech.* **34**, 375–415.
- MENA, B. & CASWELL, B. 1974 Slow flow of an elastic-viscous fluid past an immersed body. *Chem. Engng J.* **8**, 125–134.
- METZNER, A. & ASTARITA, G. 1967 External flows of viscoelastic materials: fluid property restrictions on the use of velocity-sensitive probes. *AIChE J.* **13** (3), 550–555.
- OLIVEIRA, P. J. 2001 Method for time-dependent simulations of viscoelastic flows: vortex shedding behind cylinder. *J. Non-Newton. Fluid Mech.* **101**, 113–137.
- OLIVEIRA, P., PINHO, F. & PINTO, G. 1998 Numerical simulation of nonlinear elastic flows with a general collocated finite-volume method. *J. Non-Newton. Fluid Mech.* **79**, 1–43.
- PHAN-THIEN, N. & DOU, H. 1999 Viscoelastic flow past a cylinder: drag coefficient. *Comput. Methods Appl. Mech. Engng* **180**, 243–266.
- PIPE, C. J. & MONKEWITZ, P. A. 2006 Vortex shedding in flows of dilute polymer solutions. *J. Non-Newton. Fluid Mech.* **139**, 54–67.
- PURNODE, B. & LEGAT, V. 1996 Hyperbolicity and change of type in flows of fene-p fluids. *J. Non-Newton. Fluid Mech.* **65**, 111–129.
- SAHIN, M. & OWENS, R. G. 2004 On the effects of viscoelasticity on two-dimensional vortex dynamics in the cylinder wake. *J. Non-Newton. Fluid Mech.* **123**, 121–139.
- SIBILLA, S. & BARON, A. 2002 Polymer stress statistics in the near-wall turbulent flow of a drag-reducing solution. *Phys. Fluids* **14**, 1123–1136.
- STONE, P., ROY, A., LARSON, R., WALEFFE, F. & GRAHAM, M. 2004 Polymer drag reduction in exact coherent structures of plane shear flow. *Phys. Fluids* **16** (9), 3470–3482.
- SURESHKUMAR, R. & BERIS, A. 1995 Effect of artificial stress diffusivity on the stability of numerical calculations and the flow dynamics of time-dependent viscoelastic flows. *J. Non-Newton. Fluid Mech.* **60**, 53–80.
- SURESHKUMAR, R., BERIS, A. N. & HANDLER, R. A. 1997 Direct numerical simulation of the turbulent channel flow of a polymer solution. *Phys. Fluids* **9** (3), 743–755.
- TOWNSEND, P. 1980 A numerical simulation of newtonian and visco-elastic flow past stationary and rotating cylinders. *J. Non-Newton. Fluid Mech.* **6**, 219–243.
- ULTMAN, J. & DENN, M. 1971 Slow viscoelastic flow past submerged objects. *Chem. Engng J.* **2**, 81–89.
- USUI, H., SHIBATA, T. & SANO, Y. 1980 Kármán vortex behind a circular cylinder in dilute polymer solutions. *J. Chem. Engng Japan* **13** (1), 77–79.

- WAPPEROM, P. & WEBSTER, W. 1999 Simulation for viscoelastic flow by a finite volume/element method. *Comput. Methods Appl. Mech. Engng* **180**, 281–304.
- WILLIAMSON, C. H. K. 1996a Three-dimensional wake transition. *J. Fluid Mech.* **328**, 345–407.
- WILLIAMSON, C. H. K. 1996b Vortex dynamics in the cylinder wake. *Annu. Rev. Fluid Mech.* **28**, 477–539.
- ZDRAVKOVICH, M. M. 1997 *Flow Around Circular Cylinders Volume 1: Fundamentals*. Oxford University Press.